Volume 1 | Number 1 | Jan 2013 | Pages 1–100

Journal of
Materials Chemistry A

Materials for energy and sustainability
www.rsc.org/materialsA

Li⁺

ROYAL SOCIETY
OF CHEMISTRY

ROYAL SOCIETY
OF CHEMISTRY

www.rsc.org/materialsA

Journal Name

ARTICLE

Phosphorus/N-doped Carbon Nanofiber Composite as Anode Material for Sodium-Ion Batteries

Boyang Ruan, Jun Wang, Dongqi Shi, Yanfei Xu, Shulei Chou, Huakun Liu, Jiazhao Wang*

Sodium-ion batteries (SIBs) have been attracting intensive attention at present as the most promising alternative to lithium-ion batteries in large-scale electric storage applications, due to the low-cost and natural abundance of sodium. Elemental phosphorus (P) is very promising anode material for SIBs, with the highest theoretical capacity of 2596 mAh g^{-1}. Recently, there have been many efforts devoted to phosphorus anode materials for SIBs. As pure red phosphorus can not react with Na reversibly, many attempts to prepare composite materials containing phosphorus have been reported. Here, we report the facile preparation of a red phosphorus/N-doped carbon nanofiber composite (P/NCF) that can deliver a reversible capacity of 731 mAh g^{-1} in sodium-ion batteries (SIBs), with capacity retention of 57.3 % over 55 cycles. Our results suggest that it would be a promising anode candidate for SIBs with a high capacity and low cost.

1. Introduction

For large scale applications of renewable power stations and smart grids, cost-effective energy storage and conversion devices are highly desirable. In this regard, owing to their low cost, the abundant natural resources of sodium,[1-6] and the similar chemistry of sodium and lithium,[7-9] sodium ion batteries (SIBs) have received increasing attention.[10-25] Although SIBs are a promising alternative to lithium ion batteries (LIBs) in large-scale applications, the critical problem of lower energy density limits the further development of SIBs. It is an especially great challenge to obtain a promising anode material for SIBs, because the commercial graphite used in LIBs is not suitable for SIBs due to the larger size of the sodium ion compared to the lithium ion. Recently, elemental phosphorus (P) was found to be an attractive anode material,[26-28] as it can give a high theoretical specific capacity of 2596 mAh g^{-1} to form the Na_3P phase.[29] In addition to the high capacity, utilization of phosphorus as an anode material has the advantages of natural abundance and low cost. Phosphorus shows great potential as anode material for the next generation of sodium batteries, which should be capable of offering high energy density as power sources at low cost. It has been reported, however, that sodium batteries with P as anode have some problems related to the low utilization

efficiency of the active materials and poor cycle life.[30] This is because red phosphorus has very low electrical conductivity (1×10^{-14} S/cm),[31] which leads to poor electrochemical accessibility and low utilization of the phosphorus in the electrode. Studies of the Na-P binary system have indicated that each phosphorus atom can accommodate up to 3 sodium atoms, leading to the formation of Na_3P phase, accompanied by a volume expansion of 300%.[32-35] This huge volume change would give rise to the disintegration of the electrode and loss of electronic contact between the P particles, resulting in the formation of cracks, followed by pulverization of the active mass particles and permanent capacity loss.

To solve the problems of the low conductivity, and large volume changes in P anodes, several research efforts have been focused on the development of composites consisting of phosphorus and carbonaceous materials, which have yielded better capacity retention and cycle life than pure P anodes.[32-34,36] Its relatively low mass, good electronic conductivity, reasonable Na-insertion capability, and small volume expansion, coupled with softness and compliance, make carbon the best active matrix.[37,38]

The pioneering research on P anodes was conducted by Yang's[32] and Lee's[33] groups, who developed phosphorus anodes through the high-energy ball-milling of red phosphorus and carbon black. Yang and co-workers reported that amorphous red phosphorus/carbon composites could deliver a high capacity of 1764 mAh g^{-1} at the current density of 250 mA g^{-1}.[32] Lee's group's study presented a slightly higher capacity of 1890 mAh g^{-1} at a lower current density of 143 mA g^{-1} with 30 cycles of battery performance.[33] Our group recently prepared high-performance composites by simply hand-grinding

Institute for Superconducting and Electronic Materials, University of Wollongong, NSW 2500, Australia. E-mail: jiazhao@uow.edu.au; Fax: +61 2 4221 5731; Tel: +61 2 4298 1478.

commercial microscale red phosphorus and carbon nanotubes, and the as-prepared composites could deliver a reversible capacity of 1675 mAh g^{-1}.[34]

Inspired by these examples of success, we have prepared phosphorus/N-doped carbon nanofiber composites (P/NCF) in this work by using N-doped carbon and red phosphorus via an evaporation/deposition strategy. Compared with the ball-milling method for preparing phosphorus/carbon composite, the vaporization-condensation method has more advantages, such as uniform adsorption of the phosphorus, keeping the original morphology of N-doped carbon fibers, *etc*. There have been many reports on using N-doped carbon as an efficient strategy to improve the electrochemical performance of carbon-based both Li-storage and Na-storage anodes.[39-43] In the N-doped carbon which is derived from the precursor of polypyrrole (PPy), the presence of nitrogen species on the carbon surface can lead to a pseudo capacitive interaction between the electrolyte ions and the nitrogen-containing functional groups because of its heteroatomic defects. On the other hand, the structure of the porous-fiber in our N-doped carbon is another attractive characteristic for composite formulations, in such aspects as enhancing capacity, surface wettability, and electronic conductivity.[44] Based on the above advantages, we used PPy precursor as the source of carbon, then sintered it in argon atmosphere to obtain N-doped carbon nanofibers, and further obtained phosphorus/N-doped carbon nanofiber composite (P/NCF) by loading with phosphorus. The P/NCF exhibited capacity as high as 731 mAh g^{-1} at 100 mA g^{-1} after 55 cycles. In this paper, we refer to the specific capacity of P/NCF composite based on red phosphorus.

2. Experimental

2.1 Synthesis of N-doped carbon nanofibers

The starting materials, cetyltrimethylammonium bromide (CTAB), pyrrole, ammonium persulfate (APS), and red phosphorus were purchased from Australia Sigma-Aldrich Pty. Ltd. All the chemicals were of analytical grade and used as purchased without further treatment. The precursor polypyrrole (PPy) was synthesized by the solution chemistry method.[45] The synthetic process was as follows: 0.72 g CTAB was dissolved in 200 ml deionized water, and 0.33 g pyrrole was added into the CTAB solution and ultrasonically vibrated for 5 minutes. Then, a solution of 1.13 g APS dissolved in 20 ml deionized water was added into the previous solution and stirred for 24 h at room temperature. A black precipitate (PPy nanofibers) was obtained by centrifuging. The PPy nanofibers were dried overnight at 80 °C in an oven under vacuum. The as-synthesized PPy was heated to 600 °C at a heating rate of 5 °C min^{-1} and kept for 4 h under an argon atmosphere in a tube furnace to form nitrogen-doped carbon nanofiber webs.
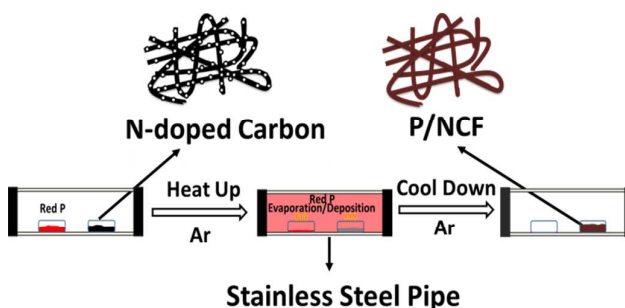
2.2 Preparation of P/NCF

Red phosphorus was washed with distilled water to remove any oxides before processing. Red phosphorus (0.2 g) and N-doped carbon (0.2 g) were placed in a sealed stainless steel pipe, which was filled with pure argon. The stainless steel pipe was first heated to 450 °C with a heating rate of 5 °C min^{-1} in a tube furnace, and kept at that temperature for 3 h. During this time, the stainless pipe was filled with phosphorus vapour (see Scheme 1). Subsequently, the stainless steel pipe was cooled to 260 °C at the cooling rate of 1 °C min^{-1} and then held at that temperature for 18 h. The aim of this step was to reduce the speed at which vaporized phosphorus atoms condense into solid state and avoid forming white phosphorus. Phosphorus exists in the gas-liquid-solid triple point state at 260 °C. Maintaining this step for a long time, will also help to impregnate the phosphorus into the pores of the N-doped carbon fibers so as to complete the evaporation/deposition process. Finally, P/NCF was obtained by cooling the stainless steel pipe to room temperature. Scheme 1 clearly displays the above preparation process.

2.3 Characterization

The structure of the obtained P/NCF and precursors was characterized by powder X-ray diffraction (XRD; GBC MMA diffractometer) with Cu Kα radiation at a scan rate of 4° min^{-1}. Raman spectra were collected using a JOBIN Yvon Horiba Raman spectrometer model HR800, with a 10 mW helium/neon laser at 632.8 nm excitation in the range of 200 to 2000 cm^{-1}. Thermogravimetric analysis (TGA) measurements were carried out in flowing argon at a heating rate of 5° C min^{-1} using a Mettler Toledo TGA/DSC1. X-ray photoelectron spectroscopy (XPS) was conducted using a SPECS PHOIBOS 100 Analyser installed in a high-vacuum chamber with the base pressure below 10^{-8} mbar, X-ray excitation was provided by Al Kα radiation with photon energy hv = 1486.6 eV at the high voltage of 12 kV and power of 120 W. The XPS binding energy spectra were recorded with the pass energy of 20 eV in the fixed analyser transmission mode. Analysis of the XPS data was carried out using the commercial Casa XPS 2.3.15 software package. All the spectra were calibrated by C$_{1s}$=284.6 eV. The Brunauer-Emmett-Teller (BET) surface area and pore size distribution (PSD) were measured by nitrogen adsorption/desorption using a Quantachrome Autosorb-IQ MP instrument. The morphology of the samples was investigated by field-emission scanning electron microscopy (FESEM; JEOL JSM-7500FA).

Scheme 1. Schematic illustration of the preparation of P/NCF

2.4 Electrochemical Measurements

The electrochemical measurements were conducted using 2032-type coin cells. The working electrode was prepared by coating a slurry containing 80 wt% active materials, 10 wt% Super-P (carbon black), and 10 wt% carboxymethyl cellulose (CMC) binder on a copper foil substrate. Then, the electrode film was dried in a vacuum oven at 80 °C overnight. The electrolyte used in this work was 1.0 mol L^{-1} NaClO$_4$ in an ethylene carbonate (EC) − diethyl carbonate (DEC) solution (1:1 v/v), with 5 wt% addition of fluoroethylene carbonate (FEC). All the cells were assembled in a glove box filled with argon and tested at room temperature. The galvanostatic charge/discharge testing was conducted on a Land Test System with a cut-off voltage range of 0 − 2.5 V (vs. Na/Na$^+$) at a constant current of 100 mA g^{-1}. Cyclic voltammetry measurements were conducted at a scan rate of 0.1 mV s^{-1} on a SP-300 POTENTIONSTAT GALVANOSTAT electrochemical workstation.

Figure 1. XRD patterns (a), Raman spectra (b)，and TGA curves (c) of red phosphorus, N-doped carbon, and P/NCF.

3. Results and Discussion

Figure 1a, shows the X-ray diffraction (XRD) patterns of the commercial red P, N-doped carbon, and P/NCN. For the red P, the peaks centred at 15° and 34° are attributed to the d$_{013}$ and d$_{31-8}$ planes.[40-41] For the N-doped carbon, the diffraction peak at 24.5°, corresponds to d-spacing of 0.36 nm, which is very close to 0.34 nm, i.e., the d$_{002}$ plane in graphite.[43] In the P/NCF pattern, there is a broad peak at 24.5°, which is considered to be a merger of N-doped carbon and red P peaks, and a characteristic peak of red P is also clearly observed at 15°, although the intensity is weak. These peaks confirm the presence of red P in the composite. Figure 1b shows the Raman spectra of red P, N-doped carbon and P/NCF. In the spectrum of amorphous red phosphorus, there are three bands from 300 to 500 cm^{-1}, which are characteristic peaks of red P.[40] The red P largely consists of P$_7$ and P$_9$ cages arranged to form pentagonal tubes in paired layers; P$_9$ cages are considered to be responsible for the sharp peak at approximately 350 cm^{-1}. The G mode of N-doped carbon (~ 1580 cm^{-1}) involves an E$_{2g}$ symmetrical bond stretching motion of pairs of C sp^2 atoms, while the D band (~ 1350 cm^{-1}) is attributed to the breathing mode of six-membered rings.[44] The Raman pattern of P/NCF exhibits the two characteristic peaks at 1350 cm^{-1} and 1580 cm^{-1}, which are attributed to N-doped carbon. The Raman intensity and wavenumber of both the D- and G-bands are unchanged in the spectrum of P/NCF, indicating that the carbon matrix and the adsorbed phosphorus have no interaction in P/NCF. Also, we can see that the three bands from 300 to 500 cm^{-1}, the characteristic peaks of red phosphorus, weakly appear in the composite. These traces, evident in range of 350-480 cm^{-1}, verify the presence of elemental phosphorus in the composite. This result is in accordance with the conclusion drawn from the XRD and XPS.

The thermogravimetric analysis (TGA) curve of P/NCF is shown in Figure 1c. There is an obvious weight loss at about 450 °C under argon atmosphere, a much higher temperature than for the pure red phosphorus, which shows a clear weight loss at about 410 °C, the temperature at which red phosphorus sublimes. This high temperature indicates that phosphorus in the composite is relatively more stable than elemental phosphorus, which is due to the adsorption of phosphorus on the surface of the carbon. The content of P in the P/NCF was determined from the TGA curves to be about 27.5 wt %.

X-ray photoelectron spectroscopy (XPS) was used to further investigate the interaction between the PPy, N-doped carbon and red phosphorus. In Figure 2, the deconvolution of the N1s spectrum identifies the surface functionalities of PPy (Fig. 2a), N-doped carbon (Fig. 2b) and P/NCF (Fig. 2c). There is only one fitted component peak at 400.4 eV for PPy, which is attributed to pyrrolic nitrogen. Regarding the N-doped carbon, there are three fitted component peaks at 397.9, 398.9, and 399.8 eV, which are assigned to pyridinic (N-6), pyrrolic/pyridone (N-5), and quaternary (N-Q) nitrogen, respectively. This sequence is consistent with the literature.[46] For P/NCF, The sequence of N-6, N-5 and N-Q peak is same as in N-doped carbon. There are
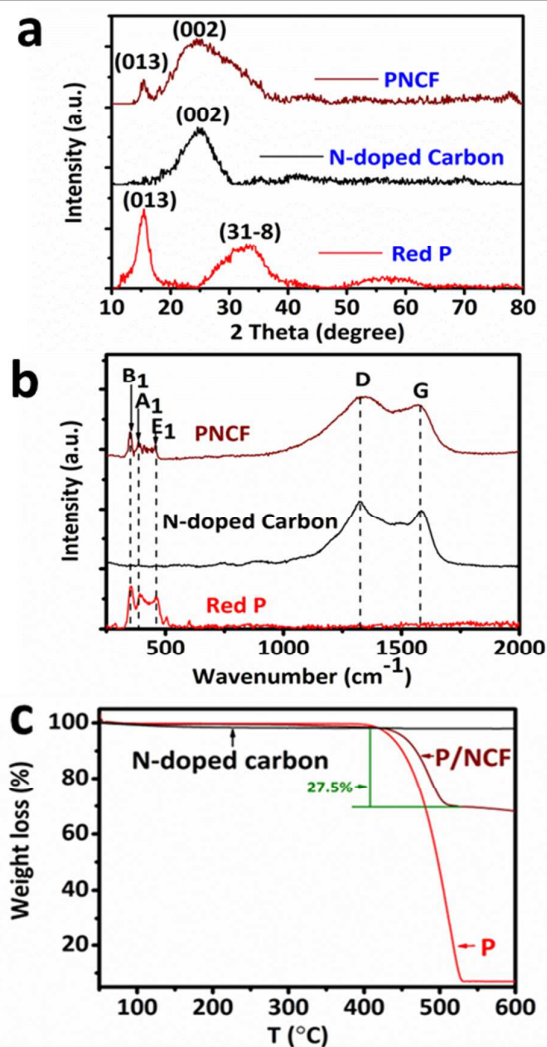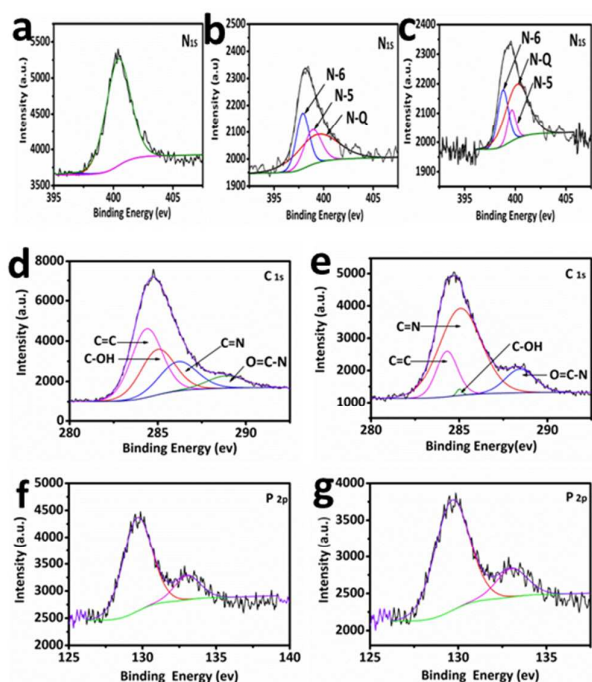
Figure 2. High resolution N_{1s} XPS spectra of PPy (a), N-doped carbon (b) and P/NCF (c). C_{1s} XPS spectra of N-doped carbon (d) and P/NCF (e). P 2p XPS spectra of red P (f) and P/NCF (g).
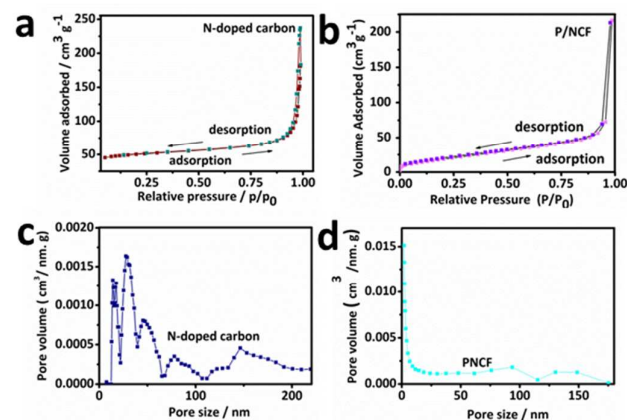

Figure 3. Porosity characterization of N-doped carbon (a)，and P/NCF (b) by N_2 adsorption-desorption isotherms. Pore size distribution of N-doped carbon (c), and P/NCF (d).

Table 1 Key pore characteristics of N-doped carbon and P/NCF.

Material	Surface area $(m^2\ g^{-1})$	Pore volume $(cm^3\ g^{-1})$	Average pore size (nm)
N-doped carbon	158.0	0.34	17.7
Phosphorus	2.5	0.009	
P/NCF	75.6	0.28	7.2

only some changes of intensities. In N-doped carbon, the C_{1s} spectrum can be fitted into the following bands: C=C (284.5 eV), C–OH (285.4 eV), C sp^2 linked to N (285.9 eV), and C doubly bound to O and singly to C (287.6 eV) (Fig.2c).[46, 47] In the case of the C_{1s} spectrum in the P/NCF composite, the intensity of some peaks apparently changed due to the effects on bonding of the encapsulation of the P (Fig.2d).Two peaks centered at 129.8 and 134.0 eV were observed in the P_{2p} XPS spectrum of the phosphorus (Fig.2e). The peak at 129.8 eV is attributed to $P_{2p}^{3/2}$, and the other one, which has relatively low intensity at 134.0 eV, may come from phosphates.[48] In the case of P/NCF, there was no significant change in the positions of the P peaks, but the intensity clearly decreased (Fig.2f). Here, we also measured the C, N and O contents in PPy fibers and N-doped carbon fibers by XPS. The mass concentration for PPy was C_{1s} 68.58%, N_{1s} 19.23%, O_{1s} 12.18%. As for N-doped carbon, it was following, C_{1s} 78.69%, N_{1s} 9.64%, O_{1s} 11.67%. From these data,
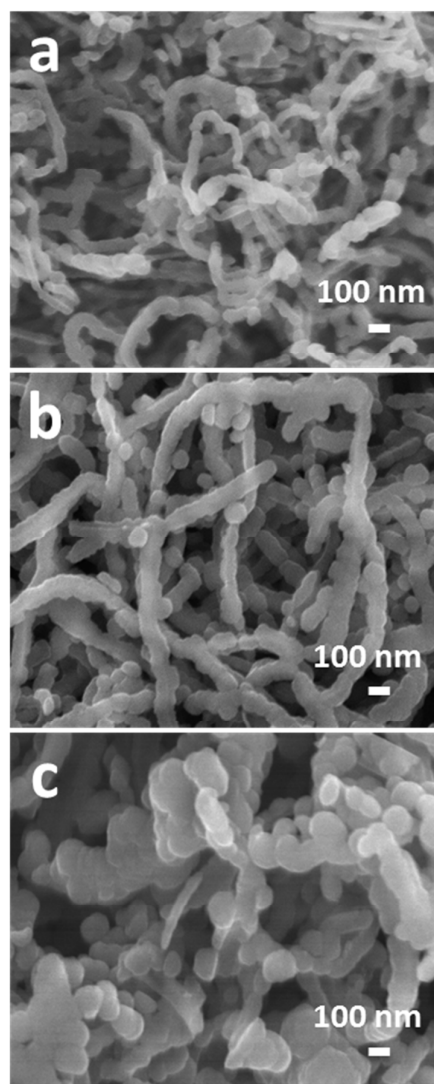

Figure 4. SEM images of the samples: PPy (a), N-doped carbon (b), and P/NCF (c)

we can see that the N content decreased significantly due to the pyrolysis of PPy.

In this paper, we used the Quantachrome Autosorb-iQ MP to measure the BET surface, pore size distribution of N-doped carbon and composite P/NCF with BJH model. As shown in Figure 3a, N_2 adsorption–desorption isotherms of N-doped carbon can be identified as type IV isotherms in the International Union of Pure and Applied Chemistry (IUPAC) classification with a typical mesoporous hysteresis loop. The adsorption–desorption hysteresis of N-doped carbon is very clear, suggesting that it possesses a large volume of mesopores. This conclusion is fully supported by the pore size distribution curves obtained from the N_2 isotherms based on density functional theory calculations (Fig.3c). The porosity data, including the BET surface area, pore volume, and average pore diameter for all samples are summarized in Table 1.

N-doped carbon presents a high surface area of 158 $m^2 g^{-1}$ and a large pore volume of 0.34 $cm^3 g^{-1}$, with the predominant pore size around 17.7 nm, which helps to efficiently absorb and hold the phosphorus active material. It should be noted that after

loading phosphorus into the micropores or mesopores of N-doped carbon, the specific surface area and pore volume of N-doped carbon decrease rapidly, with 75.62 $m^2 g^{-1}$ and 0.28 $cm^3 g^{-1}$ retained, respectively. This indicates that most of the nanopores in the N-doped carbon are occupied by the element phosphorus.

The morphologies of the as-synthesized PPy, N-doped carbon and P/NCF were characterized by scanning electron microscopy (SEM), as displayed in Figure 4. The image of PPy shows a homogeneous morphology of cross-linked nanofibers less than 100 nm in diameter (Fig. 4a). After being carbonized at 600 °C for 4 h, the interconnected nanofiber structure of the PPy is still maintained (Fig. 4b). As for P/NCF, it can be seen that the diameter of the P/NCF nanofibers is larger than those of N-doped carbon (Fig. 4c). This indicates that the fibres of N-doped carbon are covered by phosphorus in P/NCF.

The Transmission electron microscopy (TEM) was further used to investigate the structure of P/NCF. As shown in Fig.5a-b. P/NCF maintains the fibrous structure of N-doped carbon, while the phosphorus impregnation has increased the average fiber diameter from less than 100 to 125 nm. These images are entirely consistent with the SEM image in Fig.4c. The TEM selected area electron diffraction (SAED) pattern in the inset of (Fig.5b) also shows a diffuse ring for the red P, which confirms its amorphous nature .[49]

The energy dispersive spectroscopy (EDS) mapping images reveal the distributions of the elements C (Fig.5d), N (Fig.5e), and P (Fig.5f) in P/NCF. In the elemental mapping of P, the points clearly demonstrate that most of the phosphorus was
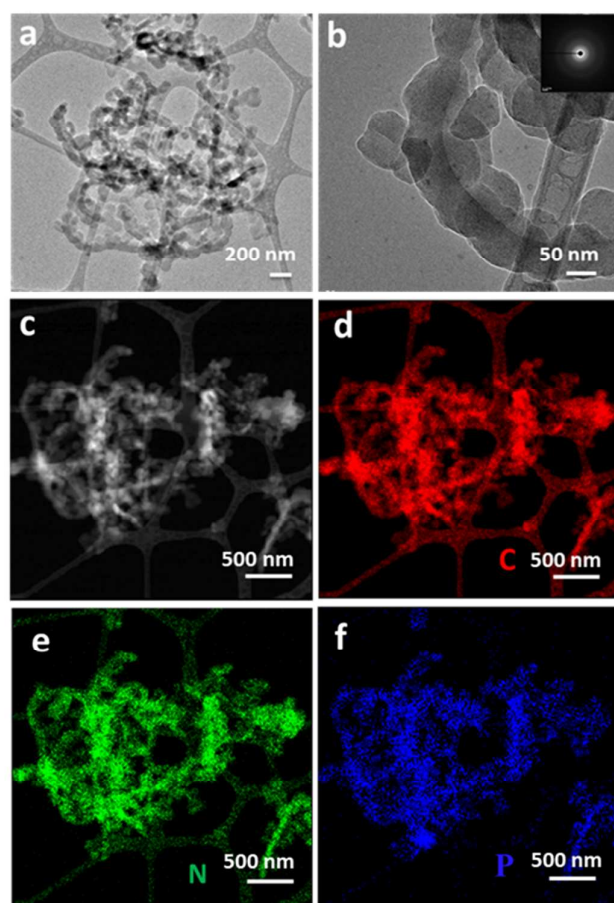

Figure 5. TEM images obtained from P/NCF: Low magnification image (a), and high magnification image, with the corresponding electron diffraction pattern shown in the inset (b). Dark background image (c) with corresponding EDS elemental mapping of C (d), N (e), and P (f).
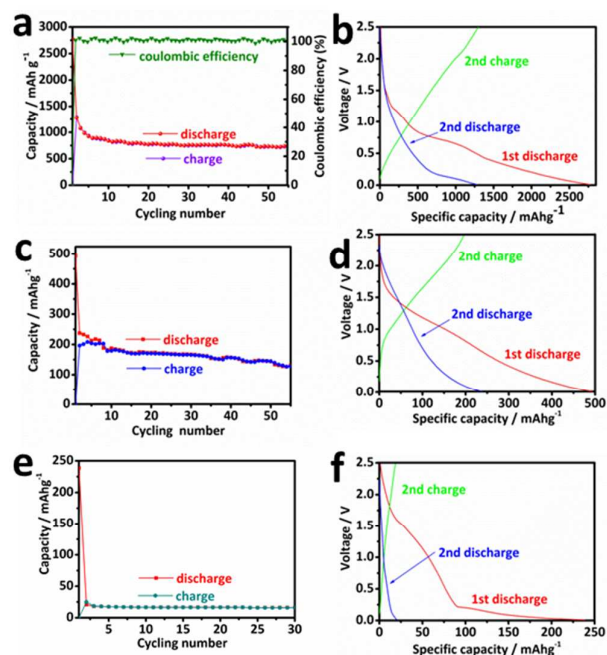

Figure 6. Cycling performance of P/NCF (a), N-doped carbon (c) and red P (e) at a current density of 100 mA g^{-1}. Charge-discharge profiles of P/NCF (b), N-doped carbon (d) and red P (e) with current density of 100 mA g^{-1}.
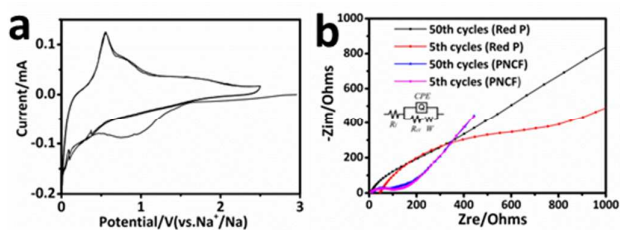
Figure 7. (a) CV curves of P/NCF scanned at a rate of 0.1mv s^{-1}. (b) Nyquist plot and equivalent circuit model of red P and P/NCF in the charged state.

homogeneously distributed in the fibers of N-doped carbon.

Figure 6 shows the cycling performances of P/NCF (a), N-doped carbon (c), and red P (e) between 2.5 V and 0 V at a current density of 100 mA g^{-1}. It can be seen that the P/NCF composite electrode exhibits a high reversible capacity of over 850 mAh g^{-1} in the first 10 cycles and maintains a reversible capacity of 731 mAh g^{-1} after 55 cycles. It and also presents excellent Coulombic efficiency of over 99.6%. The retained capacity for N-doped carbon, is approximately 130 mAh g^{-1} after 55 cycles (c). The cycling performance of red P is very low, with no more than 25 mAh g^{-1} capacity (e), even from the beginning. Figure 6, it contains the discharge/charge voltage profiles of the initial three cycles for P/NCF (b), N-doped carbon (d), and red P (f). During the first cycle, The 1st cycle discharge and 2nd cycle charge capacities of the P/NCF composite electrode are 2752 and 1275 mAh g^{-1}, respectively, giving an initial Coulombic efficiency of 46.3%. The large capacity loss of the first cycle was mainly attributed to the irreversible formation of the solid electrolyte interphase (SEI) layer on the electrode surface and irreversible Na insertion into the P/NCF matrix. Nevertheless, the capacity loss only occurs in the first few cycles, and after that, the Coulombic efficiency approaches 100%, indicating the excellent capacity retention of P/NCF. The initial discharge/charge voltage profiles for N-doped carbon display a 1st cycle discharge capacity of 493 mAh g^{-1}, and a much lower initial Coulombic efficiency of 39.8%. From the discharge/charge voltage profiles of red P, it can be seen that even in the 1st discharge state, the specific capacity is only 238 mAh g^{-1}. The initial Coulombic efficiency is merely 10.4%, so this result further demonstrates that pure red P cannot accommodate much Na^{+} insertion.

Figure 7a shows the cyclic voltammetry (CV) curves for P/NCF at a scan rate of 0.1mV/s between 0 and 2.5 V (vs Na/Na^{+}). A broad peak around 1.0 V (vs Na/Na^{+}) is observed during the first cathodic scan, which is attributed to the reduction of electrolyte to form the SEI layer. In the subsequent cathodic scans, a small weak peak around 0.4 V (vs. Na/Na^{+}), which overlaps with the SEI peak in the first cathodic scan, is observed and could be ascribed to the initial sodiation of red P. When the potential was further scanned around 0.1 V, another small sharp cathodic peak with a noticeable shoulder appeared between 0.25 and 0 V, corresponding to further sodium ion insertion. During the anodic scans, a strong peak at around 0.63 V with a shoulder at around 0.71 V and another weak peak around 1.5 V (all vs. Na/Na^{+}) are observed, which should

be attributed to the desodiation of different Na$_x$P compounds. These peaks possibly correspond to a stepwise sodium ion deinsertion from the fully charged Na$_3$P phase to form the Na$_2$P, NaP, and NaP$_7$ intermediates, respectively.[32,33]

To better understand the reason for the improved cyclability of the P/NCF electrode compared with the red P electrode, electrochemical impedance spectroscopy (EIS) of the P/NCN electrodes and red P electrodes was conducted using a sine wave of 10 mV amplitude over a frequency range of 100 kHz–0.01Hz. The Nyquist plots and the fitting model using an equivalent circuit are compared in Figure 7b, with the equivalent circuit as the inset. The plots for the P/NCF electrodes display one compressed semicircle in the high frequency region and a sloping line in the low frequency region. The intercept on the Z$_{real}$ axis in the high frequency region represents the total resistance of the electrolyte, separator, and electrical contacts (R$_i$). The semicircle in the high frequency range reflects the charge transfer resistance (R$_{ct}$), which represents the impedance associated with sodium ion transport through surface films and charge transfer at the electrode/electrolyte interface. The inclined line in the low frequency region represents the Warburg impedance (W), related to the charge transfer, by sodium ion diffusion through the material or electrolyte. *CPE* in the equivalent circuit is a constant phase element, reflecting double layer capacitance.

It can be seen that the diameters of the semicircles for P/NCF for both the 5th cycle and 50th cycle are the same, demonstrating a charge transfer resistance of 101.5 Ω, which indicates well-maintained electrical contact and a relatively stable SEI layer. This is because of the large surface area and good conductive network from the N-doped carbon, which could relieve the volume changes in the P particles during charge and discharge processes. In contrast, the charge transfer resistance (R$_{ct}$) of the cell with P electrode in the 5th cycle has a very big value of 800 Ω, which further confirms that P has very low electrical conductivity.

4. Conclusions

In summary, we have used a simple method to prepare a nanostructured phosphorus composite material (P/NCF) from N-doped carbon and red phosphorus, in which the porous carbon serves as the electronically conductive support matrix. In view of its high capacity for sodium storage, the phosphorus composite has promises for applications in electrochemical energy storage devices. The results also give clear evidence of the utility of N-doped carbon fiber for enhancing the electrochemical performance of red phosphorus as an anode material for sodium-ion batteries. This preparation strategy is simple, yet very effective, and because of its versatility, could potentially be extended to other electrically conductive support matrices for the preparation of other phosphorus composites for sodium-ion batteries.

Acknowledgements

Notes and references

1   T. Jow, L. Shacklette, M. Maxfield and D. Vernick, *J. Electrochem. Soc.*, 1987, **134**, 1730.
2   J. Barker, M. Y. Saidi and J. L. Swoyer, *U. S. Pat.*, 2005, 6,872,4.
3   B. Dunn, H. Kamath and J.-M. Tarascon, *Science*, 2011, **334**, 928.
4   N. Yabuuchi, M. Kajiyama, J. Iwatate, H. Nishikawa, S. Hitomi, R. Okuyama, R. Usui, Y. Yamada and S. Komaba, *Nat. Mater.*, 2012, **11**, 512.
5   B. L. Ellis and L. F. Nazar, *Curr. Opin. Solid State Mater. Sci.*, 2012, **16**, 168.
6   W. Deng, X. Liang, X. Wu, J. Qian, Y. Cao, X. Ai, J. Feng and H. Yang, *Sci. Rep.*, 2013, **3**.
7   D. Stevens and J. Dahn, *J. Electrochem. Soc.*, 2000, **147**, 1271.
8   S. W. Kim, D. H. Seo, X. Ma, G. Ceder and K. Kang, *Adv. Energy Mater.*, 2012, **2**, 710.
9   H. Kim, I. Park, D.-H. Seo, S. Lee, S.-W. Kim, W. J. Kwon, Y.-U. Park, C. S. Kim, S. Jeon and K. Kang, *J. Am. Chem. Soc.*, 2012, **134**, 10369.
10 Y. Cao, L. Xiao, W. Wang, D. Choi, Z. Nie, J. Yu, L. V. Saraf, Z. Yang and J. Liu, *Adv. Mater.*, 2011, **23**, 3155.
11 D. Kim, S. H. Kang, M. Slater, S. Rood, J. T. Vaughey, N. Karan, M. Balasubramanian and C. S. Johnson, *Adv. Energy Mater.*, 2011, **1**, 333.
12 V. Palomares, P. Serras, I. Villaluenga, K. B. Hueso, J. Carretero-González and T. Rojo, *Energy Environ. Sci.*, 2012, **5**, 5884.
13 J. Qian, Y. Chen, L. Wu, Y. Cao, X. Ai and H. Yang, *Chem. Commun.*, 2012, **48**, 7070.
14 D. Kim, E. Lee, M. Slater, W. Lu, S. Rood and C. S. Johnson, *Electrochem. Commun.*, 2012, **18**, 66.
15 P. Barpanda, T. Ye, S.-i. Nishimura, S.-C. Chung, Y. Yamada, M. Okubo, H. Zhou and A. Yamada, *Electrochem. Commun.*, 2012, **24**, 116.
16 J. Qian, M. Zhou, Y. Cao, X. Ai and H. Yang, *Adv. Energy Mater.*, 2012, **2**, 410.
17 J. Qian, M. Zhou and Y. Cao, *J. Electrochem*, 2012, **18**, 108.
18 Y. Lu, L. Wang, J. Cheng and J. B. Goodenough, *Chem. Commun.*, 2012, **48**, 6544.
19 M. Zhou, L. Zhu, Y. Cao, R. Zhao, J. Qian, X. Ai and H. Yang, *R. Soc. Chem. Adv.*, 2012, **2**, 5495.
20 R. Zhao, L. Zhu, Y. Cao, X. Ai and H. X. Yang, *Electrochem. Commun.*, 2012, **21**, 36.
21 S. Komaba, Y. Matsuura, T. Ishikawa, N. Yabuuchi, W. Murata and S. Kuze, *Electrochem. Commun.*, 2012, **21**, 65.
22 Y. Denis, P. V. Prikhodchenko, C. W. Mason, S. K. Batabyal, J. Gun, S. Sladkevich, A. G. Medvedev and O. Lev, *Nat.Commun.*, 2013, **4**.
23 Y.-X. Wang, S.-L. Chou, H.-K. Liu and S.-X. Dou, *Carbon*, 2013, **57**, 202-208.
24 D. Yuan, W. He, F. Pei, F. Wu, Y. Wu, J. Qian, Y. Cao, X. Ai and H. Yang, *J. Mater. Chem. A*, 2013, **1**, 3895.
25 L. Wu, X. Hu, J. Qian, F. Pei, F. Wu, R. Mao, X. Ai, H. Yang and Y. Cao, *J. Mater. Chem. A*, 2013, **1**, 7181.
26 J. Qian, X. Wu, Y. Cao, X. Ai and H. Yang, *Angewandte Chemie*, 2013, **125**, 4731.
27 W. Li, S. L. Chou, J. Z. Wang, J. H. Kim, H. K. Liu and S. X. Dou, *Adv. Mater.*, 2014, **26**, 4037.
28 N. Yabuuchi, Y. Matsuura, T. Ishikawa, S. Kuze, J. Y. Son, Y. T. Cui, H. Oji and S. Komaba, *ChemElectroChem*, 2014, **1**, 580.
29 J. M. Sangster, *J. Phase Equilib. Diff.*, 2010, **31**, 62.
30 C. Marino, A. Debenedetti, B. Fraisse, F. Favier and L. Monconduit, *Electrochem. Commun.* 2011, **13**, 346.
31 P. Extance and S. Elliott, *Philos. Mag. B*, 1981, **43**, 469.
32 H. Capacity, *Angewandte Chemie, International Edition*, 2013, **52**, 4633.
33 Y. Kim, Y. Park, A. Choi, N. S. Choi, J. Kim, J. Lee, J. H. Ryu, S. M. Oh and K. T. Lee, *Adv. Mater.*, 2013, **25**, 3045.
34 W.-J. Li, S.-L. Chou, J.-Z. Wang, H.-K. Liu and S.-X. Dou, *Nano Lett.*, 2013, **13**, 5480.
35 L. Wang, X. He, J. Li, W. Sun, J. Gao, J. Guo and C. Jiang, *Angewandte Chemie International Edition*, 2012, **51**, 9034.
36 J. Song, Z. Yu, M. L. Gordin, S. Hu, R. Yi, D. Tang, T. Walter, M. Regula, D. Choi and X. Li, *Nano Lett.*, 2014, **14**, 6329.
37 S. H. Ng, J. Wang, D. Wexler, K. Konstantinov, Z. P. Guo and H. K. Liu, *Angewandte Chemie, International Edition*, 2006, **45**, 6896.
38 N. Kurita and M. Endo, *Carbon*, 2002, **40**, 253.
39 W. H. Shin, H. M. Jeong, B. G. Kim, J. K. Kang and J. W. Choi, *Nano Lett.*, 2012, **12**, 2283.
40 G. Lota, K. Fic and E. Frackowiak, *Energy Environ. Sci.*, 2011, **4**, 1592.
41 H. g. Wang, Z. Wu, F. l. Meng, D. l. Ma, X. l. Huang, L. m. Wang and X. b. Zhang, *ChemSusChem*, 2013, **6**, 56.
42 L. Fu, K. Tang, K. Song, P. A. van Aken, Y. Yu and J. Maier, *Nanoscale*, 2014, **6**, 1384.
43 Z. Wang, L. Qie, L. Yuan, W. Zhang, X. Hu and Y. Huang, *Carbon*, 2013, **55**, 328.
44 Z.-S. Wu, W. Ren, L. Xu, F. Li and H.-M. Cheng, *ACS Nano*, 2011, **5**, 5463.
45 G. Fuge, P. May, K. Rosser, S. Pearce and M. Ashfold, *Diamond and Related Materials*, 2004, **13**, 1442.
46 46.P. Burg, P. Fydrych, D. Cagniant, G. Nanse, J. Bimer and A. Jankowska, *Carbon*, 2002, **40**, 1521.
47 Y. Mao, H. Duan, B. Xu, L. Zhang, Y. Hu, C. Zhao, Z. Wang, L. Chen and Y. Yang, *Energy Environ. Sci.*, 2012, **5**, 7950.
48 J. Sun, G. Zheng, H.-W. Lee, N. Liu, H. Wang, H. Yao, W. Yang and Y. Cui, *Nano Lett.*, 2014, **14**, 4573.
49 C. M. Park and H. J. Sohn, *Adv. Mater.*, 2007, **19**, 2465.